Topological Magnonics: A Paradigm for Spin-Wave Manipulation and Device Design

X. S. Wang,[1,2] H. W. Zhang,[1] and X. R. Wang[2,3,*]

[1]School of Electronic Science and Engineering and State Key Laboratory of Electronic Thin Film and Integrated Devices, University of Electronic Science and Technology of China, Chengdu, Sichuan 610054, China

[2]Department of Physics, The Hong Kong University of Science and Technology, Clear Water Bay, Kowloon 999077, Hong Kong

[3]HKUST Shenzhen Research Institute, Shenzhen 518057, China

(Received 7 June 2017; revised manuscript received 29 June 2017; published 27 February 2018)

Conventional magnonic devices use magnetostatic waves whose properties are sensitive to device geometry and the details of magnetization structure, so the design and the scalability of the device or circuitry are difficult. We propose topological magnonics, in which topological exchange spin waves are used as information carriers, that do not suffer from conventional problems of magnonic devices with additional nice features of nanoscale wavelength and high frequency. We show that a perpendicularly magnetized ferromagnet on a honeycomb lattice is generically a topological magnetic material in the sense that topologically protected chiral edge spin waves exist in the band gap as long as a spin-orbit-induced nearest-neighbor pseudodipolar interaction (and/or a next-nearest-neighbor Dzyaloshinskii-Moriya interaction) is present. The edge spin waves propagate unidirectionally along sample edges and domain walls regardless of the system geometry and defects. As a proof of concept, spin-wave diodes, spin-wave beam splitters, and spin-wave interferometers are designed by using sample edges and domain walls to manipulate the propagation of topologically protected chiral spin waves. Since magnetic domain walls can be controlled by magnetic fields or electric current or fields, one can essentially draw, erase, and redraw different spin-wave devices and circuitry on the same magnetic plate so that the proposed devices are reconfigurable and tunable. The topological magnonics opens up an alternative direction towards a robust, reconfigurable and scalable spin-wave circuitry.

DOI: 10.1103/PhysRevApplied.9.024029

I. INTRODUCTION

Spintronics concerns the generation, detection, and manipulation of spins for information storage and processing. Similar to electron spintronics, which deals with electron spin, magnon spintronics—also known as magnonics [1–3]—utilizes magnon spin, which has the advantages of low energy consumption and long coherence length [3–5]. Magnons, the quanta of spin waves, are promising information carriers, as well as a control knob of spin textures [6–8], which is the subject of intensive research in recent years. Various spin-wave devices and circuits, such as logic gates [9,10], filters [11], waveguides [12,13], diodes [14], and multiplexors [15], have been proposed and designed. The important functionality of these devices is to manipulate spin waves and to control spin-wave propagation in a designed way. In most applications, the magnetostatic surface spin waves are used as information carriers because they propagate unidirectionally so that they can transmit information in specific directions. However, although many efforts have been made [13,16], it is still difficult to effectively conduct the unidirectional magnetostatic surface spin waves in complex geometries because such spin waves require in-plane magnetization perpendicular to the spin-wave propagation direction [17]. It is desirable to have robust spin waves that are unidirectional and insensitive to device geometry and magnetization structure.

Interestingly, recently discovered magnonic topological matters [18–24] have topologically protected unidirectional spin waves that are well confined on the sample surfaces and edges, and whose propagation is very robust against internal and external perturbations, in contrast to the fragile nature of conventional spin waves. Thus, devices based on topological spin waves should not suffer from the usual problems of conventional spin-wave devices.

In this paper, we propose *topological magnonics*, in which we use topological exchange spin waves as information carriers. We first show that a perpendicularly magnetized ferromagnet on a honeycomb lattice is generically a topological magnetic material in the presence of a nearest-neighbor pseudodipolar interaction and/or a next-nearest-neighbor Dzyaloshinskii-Moriya interaction, both of which are induced by spin-orbit coupling. The topologically

*Corresponding author.
phxwan@ust.hk

protected chiral edge spin waves (TESWs) exist in the band gap and propagate in a certain direction with respect to the bulk magnetization direction, as is schematically illustrated in the left panel of Fig. 1(a). We further show that inside a domain wall that separates two domains, there are two unidirectional spin-wave modes for a given frequency in the bulk band gap due to the coupling of two TESWs, one from each domain. Both sample edges and domain walls are robust channels for conducting the TESWs, regardless of their geometries.

To explicitly demonstrate the topological magnonics concept, we design a spin-wave diode, a spin-wave beam splitter (SWBS), and a spin-wave interferometer, which are basic elements in magnonics, by using sample edges and domain walls in a topological magnetic film to manipulate the TESWs. Owing to the unidirectional property of TESWs, a segment of a sample edge can be used as a spin-wave diode. Since the TESWs propagate in opposite directions in the two domains, a TESW beam propagating towards the domain wall can neither penetrate it nor be reflected by it. It must move along the domain wall. When the spin-wave beam reaches the other edge, it will split into two beams propagating in opposite directions, as shown in the right panel of Fig. 1(a). Thus, a domain wall is essentially a 1:2 SWBS for the TESWs in the bulk band gap.

For an incoming TESW beam of a given frequency, the power division ratio of the SWBS depends on the wave numbers, the group velocities of the two modes, and the domain-wall length, but not on the position of the domain wall or the wave source because of the interference of the two spin-wave modes of the same frequency inside the domain wall. The idea can be generalized to 1-to-n spin-wave splitting. A Mach-Zehnder–type spin-wave interferometer is also designed. A spin-wave beam is first split into two, then recombined later to form an interference pattern that varies periodically with the relative phase change of the two beams.

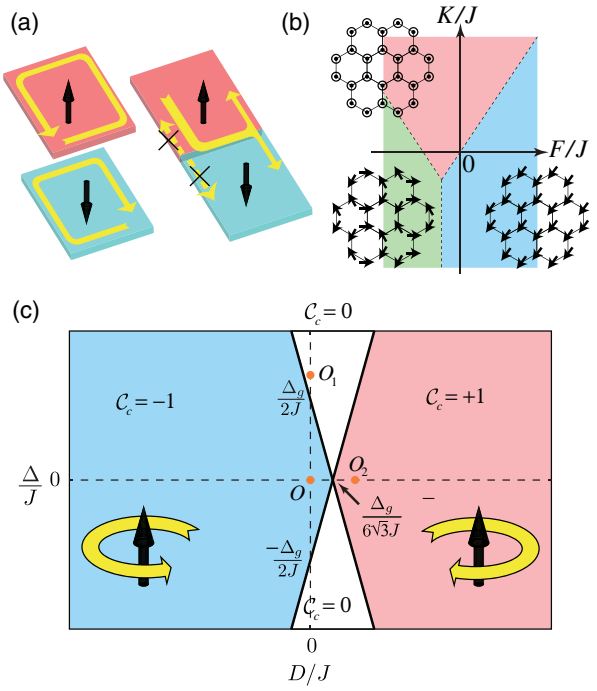

FIG. 1. (a) Schematic illustration for the TESW states (left panels) and the domain-wall SWBS (right panels). The red and cyan regions denote domains in which spins point to the $+z$ and $-z$ directions, respectively. The yellow arrows denote the spin-wave propagation direction. (b) Various phases in the K/J-F/J plane when $D=\Delta=0$. The spin arrangements in these phases are shown in the insets. (c) Topological phase diagram in the D/J-Δ/J plane (for $K=J$ and $F=0.01J$). The cyan (pink) region is a topologically nontrivial phase with the Chern number $\mathcal{C}_c=-1$ ($\mathcal{C}_c=+1$) for the conduction band, and the TESWs propagate counterclockwise (clockwise) with respect to the magnetization direction, as illustrated in the insets. The white regions represent a topologically trivial phase with $\mathcal{C}_c=0$.

II. MODEL AND ITS PHASE DIAGRAM

We consider classical spins on a honeycomb lattice of lattice constant a in the x-y plane. The Hamiltonian is

$$\mathcal{H}=-\frac{J}{2}\sum_{\langle i,j\rangle}\mathbf{m}_i\cdot\mathbf{m}_j-\frac{F}{2}\sum_{\langle i,j\rangle}(\mathbf{m}_i\cdot\mathbf{e}_{ij})(\mathbf{m}_j\cdot\mathbf{e}_{ij})$$
$$-D\sum_{\langle\langle i,j\rangle\rangle}\nu_{ij}\hat{\mathbf{z}}\cdot(\mathbf{m}_i\times\mathbf{m}_j)-\sum_i\frac{K_i}{2}m_{iz}^2, \quad (1)$$

where the first term is the nearest-neighbor ferromagnetic Heisenberg exchange interaction with $J>0$. The second and third terms arise from the spin-orbit coupling (SOC) [25,26]. $\mathbf{e}_{ij}$ is the unit vector pointing from sites i to j. The second term is the nearest-neighbor pseudodipolar interaction of strength F, which is the second-order effect of the SOC [the first-order effect, the nearest-neighbor Dzyaloshinskii-Moriya interaction (DMI), vanishes because the center of the A—B bond is an inversion center of the honeycomb lattice]. The third term is the next-nearest-neighbor DMI of strength D with $\nu_{ij}=\frac{2}{\sqrt{3}}\hat{\mathbf{z}}\cdot(\mathbf{e}_{li}\times\mathbf{e}_{lj})=\pm1$, where l is the nearest-neighbor site of i and j. The last term is the sublattice-dependent anisotropy whose easy axis is along the z direction, with anisotropy coefficients of $K_i=K+\Delta$ for $i\in A$ and $K-\Delta$ for $i\in B$. $\mathbf{m}_i$ is the unit vector of the magnetic moment of magnitude μ at site i.

The dynamics of the spins is governed by the Landau-Lifshitz-Gilbert (LLG) equation [24,27],

$$\frac{d\mathbf{m}_i}{dt}=-\gamma\mathbf{m}_i\times\mathbf{H}_i^{\text{eff}}+\alpha\mathbf{m}_i\times\frac{d\mathbf{m}_i}{dt}, \quad (2)$$

where γ is the gyromagnetic ratio and α is the Gilbert damping constant. $\mathbf{H}_i^{\text{eff}}=-(\partial\mathcal{H})/(\mu_0\mu\partial\mathbf{m}_i)$ is the effective field at site i. Out of five model parameters in Hamiltonian (1), J can be the natural energy unit. The natural units of the time, the length, and the magnetic field are $(\mu_0\mu)/(\gamma J)$, a, and $J/(\mu_0\mu)$.

The LLG equation is numerically solved by using a homemade C++ code with the fourth-order Runge-Kutta method. We first determine the ground state of the system by numerically relaxing the spins to their stable state, starting from an initial configuration in which the spins are randomly and uniformly distributed in a cone with a polar angle $\theta < 15°$. For $D = 0$ and $\Delta = 0$, the phase diagram of the model in the K/J-F/J plane is shown in Fig. 1(b). The system is in a ferromagnetic topological phase [24] with spins aligning along the z direction (the pink region) when $3J + K > -\frac{3}{2}F$ and $K > \frac{3}{2}F$. The system has a bulk band gap of $(3J + K) - \sqrt{(3J + K)^2 - 9F^2/4}$ in the case where $F \neq 0$ in this phase, with Chern number $\mathcal{C}_c = -1$ for the conduction band and $\mathcal{C}_v = +1$ for the valence band, and TESWs in the gap for a finite system. When $3J + K < -\frac{3}{2}F$ and $F < -J$ [the green region in Fig. 1(b)], the ground state has a chiral spin structure in which spins lie in the x-y plane with a zero net magnetic moment on each hexagon. As shown in the lower-left inset of Fig. 1(b), six spins on each hexagon form three ferromagnetic pairs. The spins of each pair are perpendicular to the bond of the pair, and the three pairs are in an all-in or all-out spin structure (120° from each other). For $K < \frac{3}{2}F$ and $F > -J$ (the cyan region), the system prefers an in-plane ferromagnetic state (the lower-right inset).

We focus now on the perpendicular ferromagnetic phase. To obtain the spin-wave spectrum, we assume $\mathbf{m}_i = (\delta m_{ix}, \delta m_{iy}, 1)$ to be a small deviation from the stable ground state of $\mathbf{m}_0 = (0, 0, 1)$ and substitute it into the LLG equation [27]. The linearized LLG equation is obtained by keeping only the linear terms in δm_{ix} or δm_{iy}. The Bloch theorem guarantees spin-wave eigensolutions of $\delta m_{ix} = X_\beta e^{i(\mathbf{k}\cdot\mathbf{r}_i - \omega t)}$ and $\delta m_{iy} = Y_\beta e^{i(\mathbf{k}\cdot\mathbf{r}_i - \omega t)}$, where $\beta (= A \text{ or } B)$ denotes the sublattice which site i belongs to. Then the spin wave can be obtained by solving the corresponding linearized LLG equation [28].

At the K and K' points, the gaps are $\Delta_g - 2\Delta$ and $\Delta_g + 2\Delta$, respectively, where $\Delta_g = (3J + K - 3\sqrt{3}D) - \sqrt{(3J + K + 3\sqrt{3}D)^2 - 9F^2/4}$ is the gap for $\Delta = 0$ in the presence of D. The system undergoes topological phase transitions by closing and reopening the gap at one or both valleys, as the DMI D and the staggered anisotropy Δ vary.

Figure 1(c) shows the topological phase diagram in the $D/J - \Delta/J$ plane for $K = J$ and $F = 0.01J$, which guarantees a perpendicular ferromagnetic ground state for not too large of a Δ and D ($|\Delta| < K$, so that both K_A and K_B are positive, and $|3\sqrt{3}D| < 3J + K$). The Chern number of the conduction band $\mathcal{C}_c$ is labeled in the figure, and the Chern number of the valence band $\mathcal{C}_v = -\mathcal{C}_c$ because the sum of the Chern numbers of all bands must be zero [29]. At the phase boundaries, one of the gaps closes, so we obtain two phase boundaries $\Delta = \pm\Delta_g/2$. In the cyan region, the conduction band has the Chern number -1, and each valley contributes $-1/2$. The edge states propagate counterclockwise with respect to $\mathbf{m}$. The gap at the K valley closes and reopens as one crosses the phase boundary along $D = 0$ (OO_1), and the band Chern number changes from -1 to 0, a transition from topologically nontrivial phase to trivial phase. The gaps at K and K' close and reopen at the same time when one passes $D = D_c \equiv \{(\sqrt{3}F^2)/[16(3J + K)]\}$ along $\Delta = 0$ (OO_2), and the band Chern number changes from -1 to $+1$. The system changes from one topologically nontrivial phase [the cyan region in Fig. 1(c) where the edge states propagate counterclockwise with respect to $\mathbf{m}$] to another topologically nontrivial phase [the pink region in Fig. 1(c) where the edge states propagate clockwise with respect to $\mathbf{m}$] [30]. The features of the phase diagram discussed above do not depend on specific values of F and K, as long as the ground state of the system is the perpendicular ferromagnetic state.

III. TESW AND SPIN-WAVE DIODE

To reveal the properties of TESWs at sample edges and inside a domain wall, we consider a long strip of zigzag or armchair edges with a domain wall in the middle, as illustrated in the middle panels of Fig. 2. To be specific, we consider model parameters of $D = \Delta = 0$, $K = 10J$, and $F = 5J$ so that the propagation direction of TESWs follows the right-hand rule and the domain-wall width $\sqrt{J/K} < 1$ is narrow.

The spin waves are obtained by solving the eigenvalue problem $H(k)\Psi = \omega(k)\Psi$, where $H(\mathbf{k})$ is a $4N \times 4N$ matrix, with $N = 100$ being the number of rows. The spectral function at the nth row of the strip is

$$A_n(\omega, k) = -\frac{1}{\pi}\mathrm{Im}\left(\sum_{i=0,1,2,3} G_{(4n-i)(4n-i)}\right), \qquad (3)$$

where G_{mn} is the matrix element of the Green's function $G(\omega, k) = 1/[\omega - H(k) - i\varepsilon]$, with ε being a small positive number.

The TESW modes in the bulk band gap can be clearly seen in the density plot of spectral functions shown in Fig. 2(a). The left panels are density plots of the spectral functions on the top and the bottom edges ($n = 1$ and $n = 100$). They perfectly overlap with each other, showing identical dispersion relations of TESWs in two domains. The negative slope of the $\omega(k)$ curve says that the TESWs propagate from the right to the left on both edges at the same speed. The right panels are the density plots of spectral functions inside the domain wall ($n = 50$ and $n = 51$).

Two TESW modes from the two domains denoted as $|1\rangle$ and $|2\rangle$ couple with each other inside the domain wall where they spatially overlap. The coupling results in two eigenmodes of $(|1\rangle \pm |2\rangle)/\sqrt{2}$ with different frequencies, one symmetric and the other antisymmetric with respect to

the domain-wall central line. The $\omega(k)$ curves of both modes have positive slopes, but with different values, showing the left-to-right propagation with different velocities. Importantly, these general features do not depend on the sample geometry, such as the edge types shown in Fig. 2(a): similar spin wave spectra for both a zigzag strip (the upper panel) and an armchair strip (the lower panel).

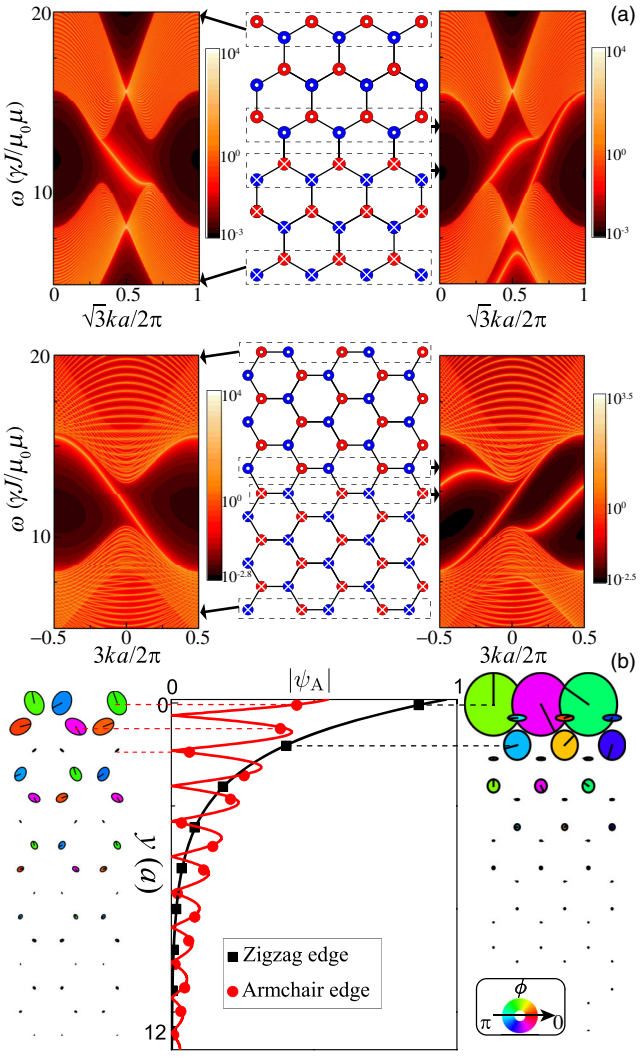

FIG. 2. (a) The density plots of the spectral function at the strip edge or domain wall (indicated by the dashed boxes) for (upper panel) a zigzag strip and (lower panel) an armchair strip. An abrupt domain wall, which separates an upper domain of $m_z = 1$ from a lower domain of $m_z = -1$, sits in the middle of each strip. (b) (Middle panel) The distribution of wave-function amplitude on sublattice A for the edge states of $\omega = 12$ along the strip-width direction (the y direction). The symbols are numerical results for a 100-wide strip, and the solid lines are the analytical results. The left (right) panel is the corresponding spatial distribution of the TESW eigenstate along the armchair (zigzag) edge. In the left and right panels, the symbol shape traces the spin-precession trajectories, and the size of the symbols denotes the amplitude of the TESW at each site. The azimuthal angles of spins on the lattice at $t = 0$ are encoded by the symbol colors with the color ring shown in the inset.

For the same frequency, the wave vectors and dispersion relations of the TESWs along different types of edges are different. The width of an edge state also depends on the type of edges. The middle panel of Fig. 2(b) shows the amplitude of the normalized TESW eigenstates for $\omega = 12$ versus the distance to the edge. The symbols represent a numerical solution of a linearized LLG equation for a 100-wide strip. The solid lines are analytical solutions of spin-wave edge-state wave function that is obtained from a spin-wave eigenequation by expanding the bulk Hamiltonian near the K point and replacing k_y by $-i\partial/\partial y$ [31].

The left and right panels of Fig. 2(b) show the spatial distributions of the TESW eigenstates for the armchair and zigzag edges, respectively. For the armchair edge, the gap locates at $k = 0$ and the edge states are more extended. For the zigzag edge, the gap locates at $k = \pi/\sqrt{3}a$, and the edge states are more localized compared to those of the armchair edge. This phenomenon is similar to the electron edge states in quantum Hall systems [32,33].

With the unidirectional property of the TESWs at the edges or inside the domain walls, we can design a spin-wave diode, which is a basic element in magnonics analogous to the p-n junction diode in electronics. Because of the intrinsic requirement of nonreciprocity for the function of a diode, magnetostatic surface waves or spin waves in the presence of DMI are used in existing designs [14]. The spin-wave diode in topological magnonics has the advantages of smaller wavelengths and better scalability.

To demonstrate the idea, we numerically solve the LLG equation with the same parameters as those specified above, and the damping is set to $\alpha = 10^{-4}$. Figure 3(a) shows a segment of an edge of a $10\sqrt{3}$-long, 15-wide sample with magnetization along the $+z$ direction. A point-source microwave field of $\mathbf{h} = 0.01[(\cos\omega t)\mathbf{e}_x + (\sin\omega t)\mathbf{e}_y]$ is applied at one of the two sites, ① or ②. We use the same model parameters as those in Fig. 2 and $\omega = 12$, which is inside the bulk band gap. Owing to the properties of TESWs, only left-going spin waves are allowed for this edge.

The upper left panel of Fig. 3(a) shows a snapshot of spin waves at $t = 5$ when the microwave field is applied at ② (the tenth site at the top edge). A spin-wave beam is excited and propagates to ① (the fifth site at the top edge), an *on* state. By contrast, when the microwave field is applied at ①, no spin wave can be detected at ②, which means an *off* state, as shown in the upper-right panel of Fig. 3(a). By tuning the DMI, the system can change from one topologically nontrivial phase to another one in which the propagation direction of the TESW is reversed, so the *on* and *off* states can also be swapped. The lower panel shows the reversal of *on* and *off* states for $D = 0.4$, with all of the other parameters unchanged. The TESW can propagate only rightward along the edge.

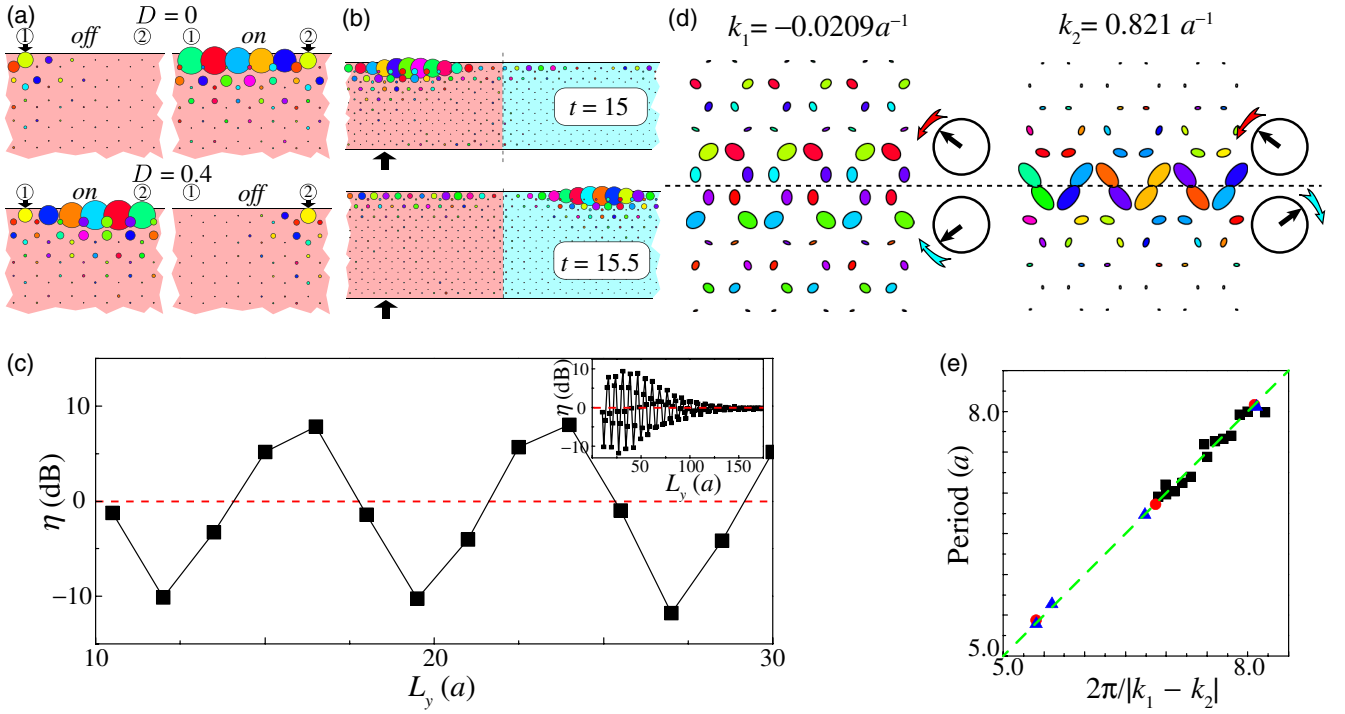

FIG. 3. (a) Snapshots of the spin waves injected at the site marked by the black arrows at $t = 5$. The upper (lower) panel is for $D = 0$ ($D = 0.4$). Only the parts between the fifth site (①) and the tenth site (②) at the top edge are shown. (b) Snapshots of a spin wave at $t = 15$ ($t = 15.5$) after leaving a 12-long (upper panel) [15-long (lower panel)] domain wall. The spin wave is injected at the site marked by the black arrow in each sample. Only the portions near the domain wall are shown. In (a) [(b)], the pink (cyan) regions represent the $m_z = +1$ ($m_z = -1$) domains. The radius of each circle is proportional to $\sqrt{m_x^2 + m_y^2}$, and the color encodes the azimuthal angles of the spins. (c) The domain-wall length dependence of spin-wave power division ratio. The symbols are simulation results, and the red dashed line is $\eta = 0$ (for a 1 : 1 splitting). (Inset) η approaches 0 for a large L_y value. (d) Spatial distribution of two topologically protected edge spin waves of $\omega = 12$ inside a domain wall parallel to the armchair edges with wave number $k_1 = -0.0209$ (left panel) and $k_2 = 0.821$ (right panel). (Insets) Spin precession is mirror symmetric (antisymmetric) as $m_\parallel \to m_\parallel$ and $m_\perp \to -m_\perp$ ($m_\parallel \to -m_\parallel$ and $m_\perp \to m_\perp$) with respect to the domain wall central line for a $k_1 = 0.0209$ ($k_2 = 0.821$) state. Here, $m_\parallel$ and $m_\perp$ are the magnetization components parallel and perpendicular to the domain wall. The meaning of the circle symbols is the same as that in Fig. 2(b). (e) The spatial period (the vertical axis) of the power division ratio from the LLG simulations verses the period of beat (the horizontal axis). The green line is $y = x$. The model parameters for squares, circles, and triangles are, respectively, $F = 5J$ and $K = 10J$, $F = 6J$ and $K = 10J$, and $F = 5J$ and $K = 9J$. α is set to 10^{-4}, and several different frequencies inside the gap are calculated for each set of parameters.

IV. SPIN-WAVE BEAM SPLITTER

A fundamental building block in spin-wave circuitry is a SWBS that can split one spin-wave beam into $n > 1$ beams. One existing SWBS is based on the interconversion between magnetostatic surface spin waves and backward volume magnetostatic spin waves in a T junction [16]. This design requires a careful control of magnetization structure near corners and edges that is not easy to achieve. Alternatively, we have suggested, without going into detail, that a domain wall in a topological magnetic material can be used as a SWBS [24].

To reveal the properties of our topological SWBS, we first calculate the power division ratio numerically. We use the same model parameters as in Fig. 2 and consider a strip that is $L_x = 40\sqrt{3}$ long and $L_y = 10.5$–180 wide. The edges along the x and y directions are zigzag and armchair types, respectively. An abrupt domain wall is placed at $x = L_x/2$. A spin-wave beam can be either injected into one sample edge from an outside source or locally generated. Here, a spin-wave pulse is locally generated by a microwave field pulse $\mathbf{h} = 0.01[(\cos\omega t)\mathbf{e}_x + (\sin\omega t)\mathbf{e}_y]$ switched on at $t = 0$ for a duration of $\Delta t = 5$. The microwave of $\omega = 12$ in the band gap is applied only at the site marked by the black arrow on the bottom edge shown in Fig. 3(b). Figure 3(b) displays snapshots of a spin-wave beam for $L_y = 12$ ($t = 15$, upper panel) and $L_y = 15$ ($t = 15.5$, lower panel). Clearly, the intensities of the two outgoing beams are not the same and depend on the strip width L_y (which is also the domain-wall length). Let us define the logarithm of the power division ratio as $\eta = \log_{10}(P_{\text{right}}/P_{\text{left}})$, where P_{right} and P_{left} are, respectively, the right and left outgoing beam powers. Then η depends on the domain-wall length, $\eta < 0$ for $L_y = 12$.

As shown in Fig. 3(c), η changes sign after the same incoming beam passing through a 15-long domain wall. Figure 3(c) shows that η oscillates periodically with L_y for a not-too-long L_y value, and it approaches 0 (1:1 splitting) for a large L_y value, as shown in the inset. Interestingly, the power division ratio does not depend on how far the wave source is from the domain wall.

To understand this oscillatory behavior, we notice that there are two TESWs for each ω in the band gap, $(|1\rangle - |2\rangle)/\sqrt{2}$ and $(|1'\rangle + |2'\rangle)/\sqrt{2}$, with different wave numbers (as discussed earlier). For $\omega = 12$, the wave numbers of the two modes are $k_1 = -0.0209$ for the antisymmetric state (and for $|1\rangle$ and $|2\rangle$) and $k_2 = 0.821$ for the symmetric one (and for $|1'\rangle$ and $|2'\rangle$), as indicated by the motion of the in-plane components of the spins on the two sides of the domain wall in the insets of Fig. 3(c).

The spatial distributions of the two chiral eigenmodes inside a domain wall parallel to the armchair edges are presented in Fig. 3(d). The mode with $k_2 = 0.821$ is highly confined around the domain wall, while the mode of $k_1 = -0.0209$ is less confined. The generated spin-wave pulse cannot be an eigenmode (an eigenmode must simultaneously exist in both domains), the spin-wave pulse must be mainly from the two eigenmodes of the same ω value and a different k value.

Since the two modes travel along the same direction at different speeds inside the domain wall, as shown earlier, their superposition generates a beat pattern with a beat wave number $k_b = (k_1 - k_2)/2$ when they overlap with each other. Thus, the power division ratio should oscillate with L_y with the period of $\lambda = |[(2\pi)/(2k_b)]| = |[(2\pi)/(k_1 - k_2)]|$. Figure 3(e) shows the period obtained from a LLG simulation (the vertical axis) against λ from the spin-wave spectrum (the horizontal axis) for different frequencies and material parameters. The simulation results coincide with the line $y = x$ quite well. For a given spin-wave pulse of time duration Δt, two eigenmodes, whose speeds inside the domain wall are v_1 and v_2, spatially separate from each other when L_y is longer than $W = |[(v_1 v_2 \Delta t)/(v_1 - v_2)]|$. Then spin waves of both eigenmodes leave the domain wall independently, and their beam power division ratios should be 1:1 since they are just single eigenmodes that are symmetric or antisymmetric under the permutation of the two edge modes of the two domains. This picture perfectly explains why η approaches 0 for a large L_y value.

The idea of the above 1:2 SWBS that uses one domain wall to control the TESWs can easily be generalized to 1-to-n SWBSs and spin-wave devices by using more domain walls (see Video 1). Figure 4 illustrates an example of a 1:4 SWBS with three domain walls that separate the $m_z = +1$ domains (the pink areas) from the $m_z = -1$ domains (the cyan areas). The gray regions are absorbing areas with a large damping constant of $\alpha = 1$. The figure shows a snapshot of the spin-wave pattern at $t = 65$ when a microwave field of frequency $\omega = 12$ is continuously applied at the site marked by the inward arrow in the bottom edge. It is clearly shown that a spin-wave beam splits into two beams by the vertically aligned domain wall, and then each of the beam is further split into two beams by the two horizontally aligned domain walls in the two arms. The domain-wall lengths are designed in such a way that the spin-wave beams are evenly split. The SWBS can also be used in series to build a complicated circuitry.

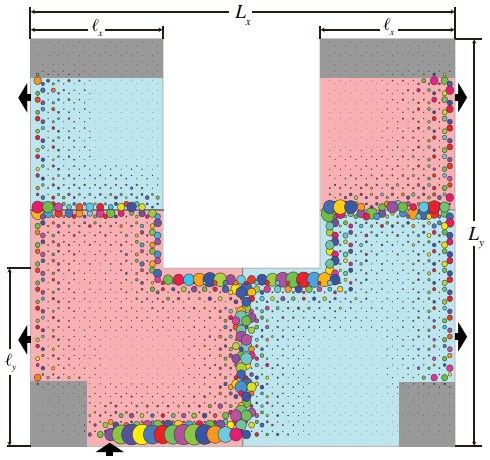

FIG. 4. A snapshot of a spin wave at $t = 65$ under a continuous microwave excitation of $\omega = 12$ at the site marked by the inward arrow on the lower edge. The outward arrows denote the output signals. The device geometry, with a zigzag edge along the x direction and armchair edges along the y direction, is $L_x = 40\sqrt{3}$, $L_y = 63$, $\ell_y = 25.5$, and $\ell_x = 12\sqrt{3}$. $\alpha = 1$ in the gray areas.

V. SPIN-WAVE INTERFEROMETER

In magnonics, it is important to manipulate the spin-wave phase because of its usefulness in information processing and logic operations [2,3,9,10]. Therefore, a spin-wave interferometer is an important element in magnonics. In topological magnonics, we can design a robust, reconfigurable spin-wave interferometer utilizing the SWBS designed above.

Figure 5(a) is a proposal of a Mach-Zehnder–type spin-wave interferometer with two domain walls separating a left $m_z = +1$ domain (the pink area) from a $m_z = -1$ domain (the cyan area). A TESW beam of $\omega = 12$ generated at the site marked by the inward arrow enters the first domain wall of length AB. The beam splits evenly to beams ① and ⑪ by the SWBS, as explained earlier. After traveling a certain distance, the two beams recombine in the second SWBS (the domain wall of length CD). Spin waves can go to either ③ or ④ (see Videos 2 and 3). Their intensities should depend on the interference of the two beams inside the second domain wall.

Figure 5(a) shows the snapshot of the spin-wave pattern at $t = 70$ when a spin-wave beam is emitted into the device at

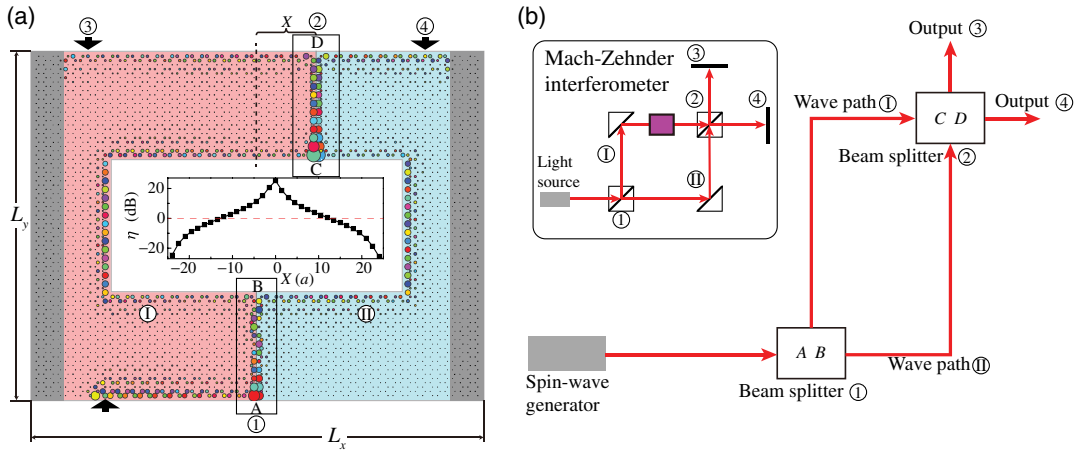

FIG. 5. (a) The spin-wave beam of $\omega = 12$, generated at the site marked by the inward arrow by a microwave field, is split into beams ① and ⑪ by the domain wall AB (the first SWBS). The two beams recombine in the domain wall CD (the second SWBS). The spin-wave pattern at $t = 70$ is represented by the size and color of the symbols, which have the same meaning as in Fig. 3. The device geometry, with armchair edges along the x direction and zigzag edges along the y direction, is $L_x = 90$ and $L_y = 40\sqrt{3}$. The first domain wall, which is $12\sqrt{3}$ long, is placed at $x = L_x/2$ and splits the incoming spin wave evenly. An area of $30 \times 6\sqrt{3}$ is removed from the center of the device so that the two split spin-wave beams can propagate along the internal boundary. The two beams recombine at the second domain wall, which is $12\sqrt{3}$ long, at X. The gray parts are absorbing areas with a large damping constant of $\alpha = 1$. (Inset) X dependence of the power division ratio η. (b) Schematic diagram of the interferometer in (a). (Inset) In the optical Mach-Zehnder interferometer, a light beam enters optical beam splitter ① and splits into two beams, ① and ⑪. The two beams recombine at the second optical beam splitter ②. The outputs ③ and ④ depend on the interference of two beams at beam splitter ②.

$t = 0$. The above process can be schematically represented by the diagram in Fig. 5(b), which is exactly the same as the diagram for the optical Mach-Zehnder interferometer shown in the inset of Fig. 5(b). Of course, instead of light and two optical beam splitters in an optical Mach-Zehnder interferometer, we have a spin wave and two SWBSs here.

In our interferometer, the relative phase of the two interfered spin waves can be tuned, for example, by placing the second domain wall at different positions or by changing the length of the second domain wall. The interference pattern is reflected by the power division ratio after the spin-wave beam comes out of the second domain wall (beam splitter ②).

The inset of Fig. 5(a) is the position ($X = 0$ when two domain walls align along the same vertical line) dependence of the power division ratio η of the second domain wall, which is $12\sqrt{3}$ long. This phenomenon is in contrast to the simple SWBS discussed earlier, whose power division ratio does not depend on the location of the domain wall. Since the position of the second domain wall can be controlled by magnetic fields or electric current or fields, this device can also be used as a tunable SWBS or a spin-wave demultiplexer. The interferometer can also be used as a sensor to measure the physical quantities that affect the spin-wave phase, such as a magnetic field.

VI. DISCUSSION, PERSPECTIVES, AND CONCLUSION

The results reported here do not depend on the details of the model as long as the system supports TESWs [18,19,21]. In practical applications, one would like to use magnetic materials with low damping such as yttrium iron garnet, whose damping can be as low as $\alpha < 10^{-5}$, so that spin-wave decay length is about 10^5 wavelengths [3,4]. We consider abrupt domain walls with strong anisotropy here, and it would be interesting to also consider a case with wide domain walls. The spin-wave interferometer shows a lot of similarities to the optical Mach-Zehnder interferometer. Although we study spin waves at a classical level in our model, it is also possible to repeat the work at quantum level so that one can investigate interesting quantum phenomena such as the magnonic Hong-Ou-Mandel effect [34].

Because of the unidirectional property of the TESWs, other basic magnonic components such as spin-wave circulators and gyrators can also be designed that utilize topological magnetic materials. Thus, our proposal may make it possible to realize fully programmable on-chip integrated circuits, a magnonic analogy of silicon-based electric integrated circuits with the advantage of reconfigurablity. It allows one to draw, erase, and redraw a complicated spin-wave circuit on a magnetic plate as one wishes since the domain configuration can be manipulated by a magnetic field and/or electric current or field. A domain configuration can be fixed with an antiferromagnetic layer through the exchange bias effect [35] if it is needed. Furthermore, the performance of the devices and circuitry can be effectively controlled and tuned by magnetic fields and electric fields through the control of material properties and domain-wall properties. Also, since the DMI can be controlled by surface engineering or an electric field [36,37], there are versatile possibilities for the design of devices.

The concepts and ideas proposed in this paper are applicable to any system that supports TESWs. Such systems are known to exist. For example, in $Lu_2V_2O_7$ with a pyrochlore structure [38] or Cu[1,3-bdc] with a kagome structure [39], there is already experimental evidence of TESWs.

To specifically realize the model studied in this paper, the lattice structure need not have a perfectly honeycomb structure. Any twisted honeycomb lattices that have two spins in one unit cell can be used, which is quite common. The pseudodipolar interaction and the Dzyaloshinskii-Moriya interaction arise from the spin-orbit interaction that exists in most magnetic materials. So heavy-metal magnetic materials are candidates for realizing our model.

For example, in A_2BO_3 materials (where A is an alkali metal and B is a transition metal), the B atoms form a honeycomb structure, and there are usually strong spin-orbit coupling effects. Ferromagnetic order is also possible for some special elements combinations or some special lattice directions [40]. β-Li_2IrO_3 is shown to possibly have a ferromagnetism and hyperhoneycomb lattice structure [41], which may be a candidate for realizing our model. AB_3 (where A is a transition metal and B is a halogen) is another family of candidate materials. A atoms form a honeycomb lattice in these materials.

There are already first-principle predictions of ferromagnetism in $NiCl_3$ and $OsCl_3$ monolayers [33,42], and the A—B—A bond is very promising for inducing a strong pseudodipolar exchange interaction. Our model may also be realized in magnonic crystals that nanomagnets are artificially arranged into a honeycomb lattice [43]. Besides the material requirements, the generation and detection of TESWs can be achieved with the same techniques used in conventional magnonic devices. For example, TESWs can be excited by an antenna that carries a microwave magnetic field and can be detected by Brillouin light-scattering spectroscopy; both are mature techniques [2,3].

In this paper, we consider small-amplitude spin waves and linear effects only. The above numerical simulations justify that the in-plane components of $\mathbf{m}$ are smaller than 0.005. There is also experimental evidence that the spin-wave amplitude is usually very small (the precession angle is less than 10 μrad at a driving field of 2000 Oe in Ref. [44]). Of course, because of the nonlinearity of the LLG equation, there are inevitably nonlinear effects, or a magnon-magnon interaction from a quasiparticle point of view, which may induce magnon band broadening and extra decay [22].

However, as long as the driving field is not too large, the nonlinear effects do not affect the applicability of our designs. When the nonlinearity starts to dominate, other interesting physics may appear, such as soliton waves analogous to those in optical fibers, which are issues for future study and not the concern of this paper.

In conclusion, we show in this paper that a perpendicularly magnetized ferromagnetic film with a pseudodipolar interaction and a Dzyaloshinskii-Moriya interaction is a generic topological magnetic material that supports TESWs. The TESWs are very useful in magnonics. An alternative paradigm of spin-wave manipulation and device design, termed topological magnonics, is proposed. Reconfigurable topological spin-wave diodes, beam splitters, and interferometers are designed and studied. The power division ratio of the spin-wave beam splitter oscillates with the domain-wall length due to the interference of two spin waves of the same frequency and different wave numbers.

ACKNOWLEDGMENTS

This work was supported by the National Natural Science Foundation of China (Grant No. 11774296) and the Hong Kong RGC (Grants No. 16300117 and No. 16301816). X. S. W acknowledges support from UESTC and the China Postdoctoral Science Foundation (Grant No. 2017M612932).

APPENDIX: EVOLUTION OF SPIN WAVES IN 1:4 SPIN-WAVE BEAM SPLITTER AND SPIN-WAVE INTERFEROMETER

In this appendix, we present movies for spin waves in a 1:4 spin-wave beam splitter and a spin-wave interferometer. The material parameters are the same as those in Figs. 2–5. The radius of each circle is proportional to the spin-wave amplitude and the color encodes the azimuthal angles of the spins, just as in Figs. 3–5.

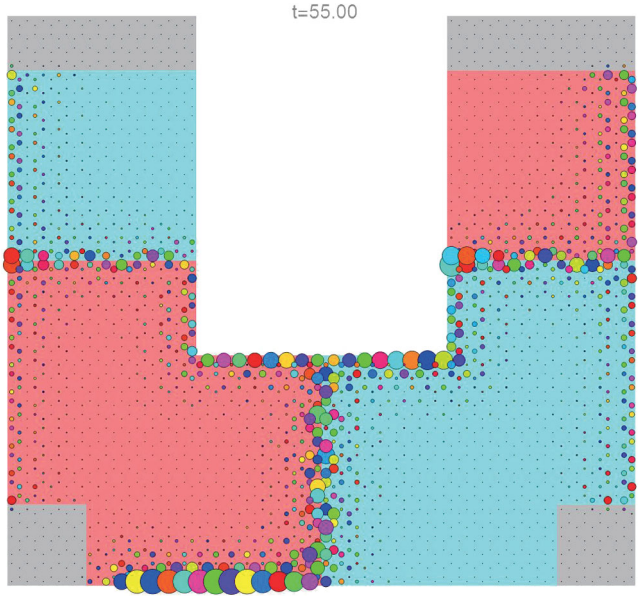

VIDEO 1. 1:4 beam splitter. The geometry is the same as in Fig. 4.

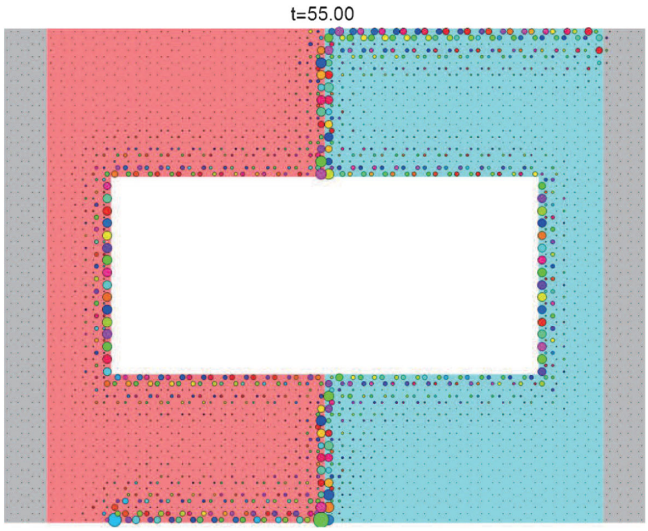

VIDEO 2. Spin-wave interferometer working at $X = 0$. The geometry is the same as in Fig. 5(a). The output spin wave goes to the right side.

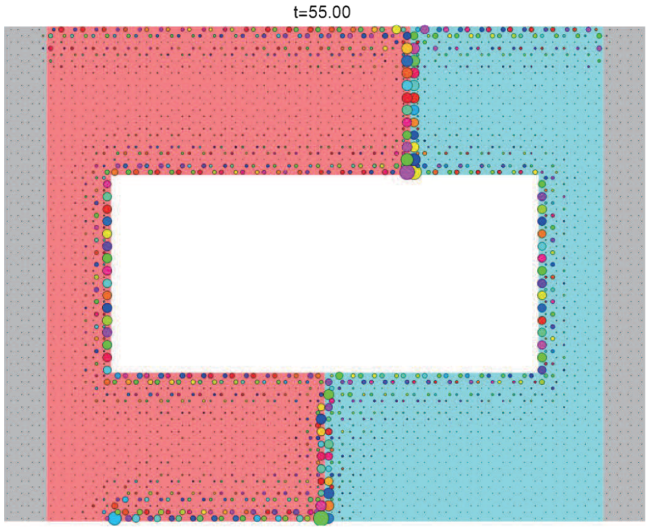

VIDEO 3. Spin-wave interferometer working at $X = 12$. The geometry is the same as in Fig. 5(a). The output spin wave goes evenly to both sides.

[1] S. O. Demokritov and A. N. Slavin, *Magnonics: From Fundamentals to Applications*, Topics in Applied Physics Vol. 125 (Springer, New York, 2013).

[2] V. V. Kruglyak, S. O. Demokritov, and D. Grundler, Magnonics, J. Phys. D **43**, 264001 (2010).

[3] A. A. Serga, A. V. Chumak, and B. Hillebrands, YIG magnonics, J. Phys. D **43**, 264002 (2010).

[4] Y. Kajiwara, K. Harii, S. Takahashi, J. Ohe, K. Uchida, M. Mizuguchi, H. Umezawa, H. Kawai, K. Ando, K. Takanashi, S. Maekawa, and E. Saitoh, Transmission of electrical signals by spin-wave interconversion in a magnetic insulator, Nature (London) **464**, 262 (2010).

[5] L. J. Cornelissen, K. J. H. Peters, G. E. W. Bauer, R. A. Duine, and B. J. van Wees, Magnon spin transport driven by the magnon chemical potential in a magnetic insulator, Phys. Rev. B **94**, 014412 (2016).

[6] P. Yan, X. S. Wang, and X. R. Wang, All-Magnonic Spin-Transfer Torque and Domain Wall Propagation, Phys. Rev. Lett. **107**, 177207 (2011).

[7] X. S. Wang, P. Yan, Y. H. Shen, G. E. W. Bauer, and X. R. Wang, Domain Wall Propagation through Spin Wave Emission, Phys. Rev. Lett. **109**, 167209 (2012).

[8] X. S. Wang and X. R. Wang, Thermodynamic theory for thermal-gradient-driven domain-wall motion, Phys. Rev. B **90**, 014414 (2014).

[9] M. P. Kostylev, A. A. Serga, T. Schneider, B. Leven, and B. Hillebrands, Spin-wave logical gates, Appl. Phys. Lett. **87**, 153501 (2005).

[10] T. Schneider, A. A. Serga, B. Leven, and B. Hillebrands, Realization of spin-wave logic gates, Appl. Phys. Lett. **92**, 022505 (2008).

[11] S.-K. Kim, K.-S. Lee, and D.-S. Han, A gigahertz-range spin-wave filter composed of width-modulated nanostrip magnonic-crystal waveguides, Appl. Phys. Lett. **95**, 082507 (2009).

[12] F. Garcia-Sanchez, P. Borys, R. Soucaille, J.-P. Adam, R. L. Stamps, and J.-V. Kim, Narrow Magnonic Waveguides Based on Domain Walls, Phys. Rev. Lett. **114**, 247206 (2015).

[13] K. Vogt, H. Schultheiss, S. Jain, J. E. Pearson, A. Hoffmann, S. D. Bader, and B. Hillebrands, Spin waves turning a corner, Appl. Phys. Lett. **101**, 042410 (2012).

[14] J. Lan, W. Yu, R. Wu, and J. Xiao, Spin-Wave Diode, Phys. Rev. X **5**, 041049 (2015).

[15] K. Vogt, F. Y. Fradin, J. E. Pearson, T. Sebastian, S. D. Bader, B. Hillebrands, A. Hoffmann, and H. Schultheiss, Realization of a spin-wave multiplexer, Nat. Commun. **5**, 3727 (2014).

[16] A. V. Sadovnikov, C. S. Davies, S. V. Grishin, V. V. Kruglyak, D. V. Romanenko, Yu. P. Sharaevskii, and S. A. Nikitov, Magnonic beam splitter: The building block of parallel magnonic circuitry, Appl. Phys. Lett. **106**, 192406 (2015).

[17] J. R. Eshbach and R. W. Damon, Surface magnetostatic modes and surface spin waves, Phys. Rev. **118**, 1208 (1960).

[18] L. Zhang, J. Ren, J.-S. Wang, and B. Li, Topological magnon insulator in insulating ferromagnet, Phys. Rev. B **87**, 144101 (2013).

[19] R. Shindou, J. I. Ohe, R. Matsumoto, S. Murakami, and E. Saitoh, Chiral spin-wave edge modes in dipolar magnetic thin films, Phys. Rev. B **87**, 174402 (2013).

[20] Alexander Mook, Jürgen Henk, and Ingrid Mertig, Edge states in topological magnon insulators, Phys. Rev. B **90**, 024412 (2014).

[21] S. A. Owerre, A first theoretical realization of honeycomb topological magnon insulator, J. Phys. Condens. Matter **28**, 386001 (2016).

[22] A. L. Chernyshev and P. A. Maksimov, Damped Topological Magnons in the Kagome-Lattice Ferromagnets, Phys. Rev. Lett. **117**, 187203 (2016).

[23] S. K. Kim, H. Ochoa, R. Zarzuela, and Y. Tserkovnyak, Realization of the Haldane-Kane-Mele Model in a System of Localized Spins, Phys. Rev. Lett. **117**, 227201 (2016).

[24] X. S. Wang, Y. Su, and X. R. Wang, Topologically protected unidirectional edge spin waves and beam splitter, Phys. Rev. B **95**, 014435 (2017).

[25] G. Jackeli and G. Khaliullin, Mott Insulators in the Strong Spin-Orbit Coupling Limit: From Heisenberg to a Quantum Compass and Kitaev Models, Phys. Rev. Lett. **102**, 017205 (2009).

[26] T. Moriya, Anisotropic superexchange interaction and weak ferromagnetism, Phys. Rev. **120**, 91 (1960).

[27] T. L. Gilbert, A phenomenological theory of damping in ferromagnetic materials, IEEE Trans. Magn. **40**, 3443 (2004).

[28] By defining $\psi_\beta^\pm = (X_\beta \pm Y_\beta)/\sqrt{2}$ (where $\beta = A,\ B$), the column vector $\Psi = (\psi_A^+, \psi_A^-, \psi_B^+, \psi_B^-)^T$ satisfies the eigenvalue problem $gH(\mathbf{k})\Psi = \omega(\mathbf{k})\Psi$, where $H(\mathbf{k})$ is a 4×4 Hermitian matrix depending on the model parameters K/J, F/J, Δ/J, D/J, and $g = \sigma_0 \otimes \sigma_3$ (with σ_0 being the 2×2 identity matrix and σ_3 the Pauli matrix).

[29] A. Bohm, A. Mostafazadeh, H. Koizumi, Q. Niu, and J. Zwanziger, *The Geometric Phase in Quantum Systems: Foundations, Mathermatical Concepts, and Applications in Molecular and Condensed Matter Physics* (Springer, Berlin, 2003).

[30] R. Matsumoto and S. Murakami, Theoretical Prediction of a Rotating Magnon Wave Packet in Ferromagnets, Phys. Rev. Lett. **106**, 197202 (2011).

[31] B. Zhou, H.-Z. Lu, R.-L. Chu, S.-Q. Shen, and Q. Niu, Finite Size Effects on Helical Edge States in a Quantum Spin-Hall System, Phys. Rev. Lett. **101**, 246807 (2008).

[32] E. Prada and G. Metalidis, Transport through quantum spin Hall insulator/metal junctions in graphene ribbons, J. Comput. Electron. **12**, 63 (2013).

[33] X.-L. Sheng and B. K. Nikolić, Monolayer of the 5*d* transition metal trichloride $OsCl_3$: A playground for two-dimensional magnetism, room-temperature quantum anomalous Hall effect, and topological phase transitions, Phys. Rev. B **95**, 201402(R) (2017).

[34] C. K. Hong, Z. Y. Ou, and L. Mandel, Measurement of Subpicosecond Time Intervals between Two Photons by Interference, Phys. Rev. Lett. **59**, 2044 (1987).

[35] W. H. Meiklejohn and C. P. Bean, New magnetic anisotropy, Phys. Rev. **105**, 904 (1957).

[36] A. Belabbes, G. Bihlmayer, S. Blügel, and A. Manchon, Oxygen-enabled control of Dzyaloshinskii-Moriya interaction in ultra-thin magnetic films, Sci. Rep. **6**, 24634 (2016).

[37] P. J. Hsu, A. Kubetzka, A. Finco, N, Romming, K. von Bergmann, and R. Wiesendanger, Electric-field-driven switching of individual magnetic Skyrmions, Nat. Nanotechnol. **12**, 123 (2017).

[38] Y. Onose, T. Ideue, H. Katsura, Y. Shiomi, N. Nagaosa, and Y. Tokura, Observation of the magnon Hall effect, Science **329**, 297 (2010).

[39] R. Chisnell, J. S. Helton, D. E. Freedman, D. K. Singh, R. I. Bewley, D. G. Nocera, and Y. S. Lee, Topological Magnon Bands in a Kagome Lattice Ferromagnet, Phys. Rev. Lett. **115**, 147201 (2015).

[40] J. Sugiyama, K. Muhai, H. Nozaki, M. Harada, M. Månsson, K. Kamazawa, D. Andreica, A. Amato, and A. D. Hillier, Antiferromagnetic spin structure and lithium ion diffusion in Li_2MnO_3 probed by μ^+SR, Phys. Rev. B **87**, 024409 (2013).

[41] T. Takayama, A. Kato, R. Dinnebier, J. Nuss, H. Kono, L. S. I. Veiga, G. Fabbris, D. Haskel, and H. Takagi, Hyperhoneycomb Iridate β-Li_2IrO_3 as a Platform for Kitaev Magnetism, Phys. Rev. Lett. **114**, 077202 (2015).

[42] J. He, X. Li, P. Lyu, and P. Nachtigall, Near-room-temperature Chern insulator and Dirac spin-gapless semiconductor: Nickel chloride monolayer, Nanoscale **9**, 2246 (2017).

[43] H.-H. Pan, H. Liu, J.-Z. Wang, J.-F. Jia, Q.-K. Xie, J.-L. Li, S. Qin, U. M. Mirsaidov, X. R. Wang, J. T. Markert, Z. Zhang, and C.-K. Shih, Quantum growth of magnetic nanoplatelets of Co on Si with high blocking temperature, Nano Lett. **5**, 87 (2005).

[44] M. Jäckl, V. I. Belotelov, I. A. Akimov, I. V. Savochkin, D. R. Yakovlev, A. K. Zvezdin, and M. Bayer, Magnon Accumulation by Clocked Laser Excitation as Source of Long-Range Spin Waves in Transparent Magnetic Films, Phys. Rev. X **7**, 021009 (2017).